Remote Phononic Effects in Epitaxial Ruddlesden−Popper Halide Perovskites

Zhizhong Chen,[†] Yiping Wang,[†] Xin Sun,[‡] Yu Xiang,[‡] Yang Hu,[†,‡] Jie Jiang,[†,§] Jing Feng,[§] Yi-Yang Sun,[∥] Xi Wang,[⊥] Gwo-Ching Wang,[‡] Toh-Ming Lu,[‡] Hanwei Gao,[⊥] Esther A. Wertz,*[,‡] and Jian Shi*[,†]

[†]Department of Materials Science and Engineering and [‡]Department of Physics, Applied Physics, and Astronomy, Rensselaer Polytechnic Institute, Troy, New York 12180, United States

[§]Faculty of Material Science and Engineering, Kunming University of Science and Technology, Kunming 650093, China

[∥]The State Key Laboratory of High Performance Ceramics and Superfine Microstructure, Shanghai Institute of Ceramics, Chinese Academy of Sciences, Shanghai 201899, China

[⊥]Department of Physics, Florida State University, Tallahassee, Florida 32306, United States

S *Supporting Information*

ABSTRACT: Despite their weak nature, van der Waals (vdW) interactions have been shown to effectively control the optoelectronic and vibrational properties of layered materials. However, how vdW effects exist in Ruddlesden−Popper layered halide perovskites remains unclear. Here we reveal the role of interlayer vdW force in Ruddlesden−Popper perovskite in regulating phase-transition kinetics and carrier dynamics based on high-quality epitaxial single-crystalline $(C_4H_9NH_3)_2PbI_4$ flakes with controlled dimensions. Both substrate−perovskite epitaxial interaction and interlayer vdW interaction play significant roles in suppressing the structural phase transition. With reducing flake thickness from ∼100 to ∼20 nm, electron−phonon coupling strength decreases by ∼30%, suggesting the ineffectiveness of phonon confinement of the natural quantum wells. Therefore, the conventional understanding that vdW perovskite is equivalent to a multiple quantum well has to be substantially amended due to significant nonlocal phononic effects in the layered crystal, where intralayer interaction is not drastically different from the interlayer force.
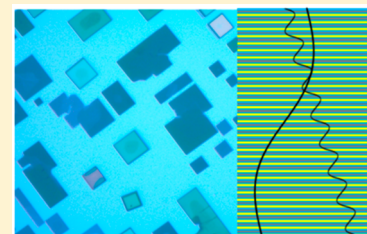
$$H_{Fr} = \sum_q -e\phi_{LO} = \sum_q \frac{ieF}{q} u_{LO}$$

Since the experimental synthesis of graphene, the library of layered materials has been growing, for example, transition-metal dichalcogenides (TMDCs), hexagonal BN (hBN), and black phosphorus.[1] Because of the lack of dangling bonds at free surface and weak interlayer van der Waals (vdW) interactions, layered materials are supposed to show negligible thickness dependence compared with nonlayered materials. Counterintuitively, as weak as vdW interactions are, the electronic, phononic, and structural properties of layered materials can be adjusted at reduced thickness such that non-layered-like behaviors are sometimes observed. For example, most TMDCs show direct-to-indirect electronic band structure transition from monolayer to multilayers.[2] An opposite trend is observed in PbI_2, where the interlayer interaction is relatively stronger.[3] In MoS_2, when the number of layers increased from 1 to 20, the Raman modes and their relative intensities varied significantly.[4] Even for graphene, where the extremely strong C−C bond stabilizes the layered structure, the Raman response of few-layer graphene still shows salient thickness dependence.[5] In addition to the interlayer interactions, vdW interaction with substrates plays a similar role as well. For example, symmetry-forbidden Raman modes in WSe_2 were activated in the WSe_2/hBN vertical heterostructure, with the new electron−phonon coupling behaviors being attributed to

the vdW interactions with hBN.[6] Surface ripples of graphene can also be suppressed by substrate vdW forces.[7] Monolayer FeSe grown on $SrTiO_3$ shows intriguing superconducting properties, and electron−phonon coupling with substrate Ti−O vibrations might be one possible mechanism.[8]

Very recently, the layered Ruddlesden−Popper (R−P) phase hybrid halide perovskites, for example, $(C_4H_9NH_3)_2PbI_4$, combining the interesting properties of layered materials and also the excellent optoelectronic/electro-optical performance of hybrid halide perovskites, have ignited new interests in the materials community.[9−14] As sketched in Figure 1a, three unique features make layered halide perovskites slightly different from conventional layered materials: (a) They consisted of alternating semiconducting lead-halide octahedron layers and insulating organic ligand layers; the self-assembled multiple quantum well (MQW) structure enables spatially confined charge carriers and huge exciton binding energy up to 300−500 meV.[12] (b) The overlap and entanglement between long organic chains may further enhance the interlayer vdW interactions and adjust structural
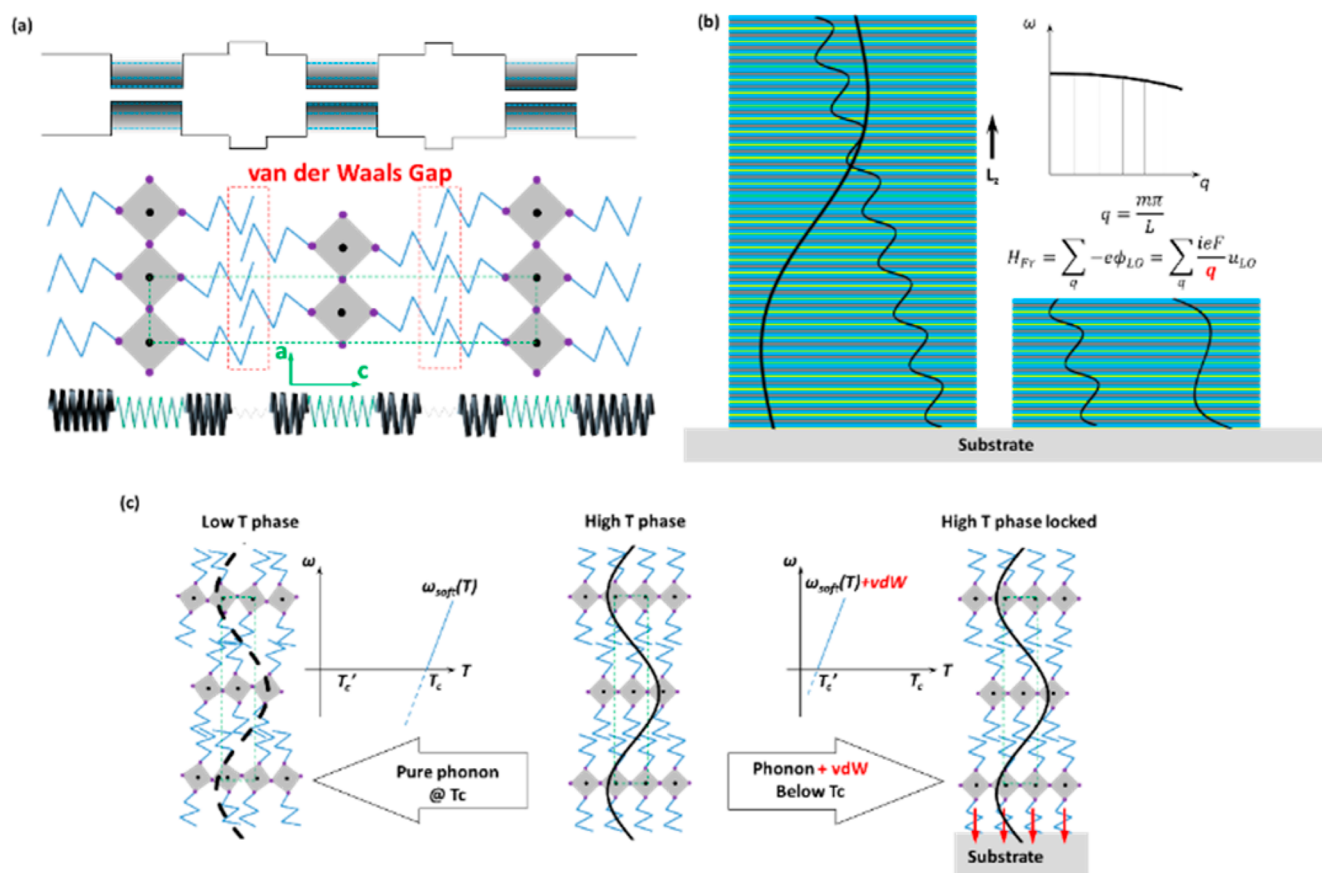
Figure 1. Electron−phonon coupling and phase transition in $(C_4H_9NH_3)_2PbI_4$. (a) From top to bottom, 2D projection of the electronic, crystal, and vibrational structures of $(C_4H_9NH_3)_2PbI_4$. Pb−I octahedrons and organic ligands are drawn as gray polyhedrons and blue jagged lines, respectively. One unit cell is marked by a green dashed line, whereas the interlayer vdW gap is marked by a red dashed line. The dark shades in the MQW structure indicate the confinement of charge carriers in Pb−I layers. In the lower drawing, organic ligands, Pb−I octahedron layers, and the vdW gap are shown as thick black, green, and thin gray springs, respectively, indicating descending vibration frequencies. (b) Possible cross-layer vibrations in $(C_4H_9NH_3)_2PbI_4$ flakes with different thickness. The vertical direction L_z is parallel to the c axis. The curves in the crystal show the amplitude and direction of vibrations, indicating that longer wavelength phonons are allowed in thicker flakes. The upper right part shows the allowed phonon wavelength in the dispersion of optical phonons. The Hamiltonian of Fröhlich interaction (H_{Fr}) is shown in the middle, where the inverse dependence with wave vector (q) is highlighted by red and ϕ_{LO} is electrostatic potential, L is well width, m is quantization number, u_{LO} is displacement of positive/negative ions, e is elementary charge, and F is material-related constant. (c) Role of vdW interactions on locking phase transition. The restoration of crystal structure, that is, the soft modes, are shown by the sinusoidal curves, and the dashed curve in low-temperature phase indicates the absence of restoration. Refer to the main text for more discussion.

phase transitions. (See Supporting Information S1 for more details.)[15] (c) The relatively small lead-halide bonding strength partially softens the layered structure, and lattice relaxation has been observed in few-layer $(C_4H_9NH_3)_2PbBr_4$ single-crystalline flakes.[16] Similar to other layered materials, electron−phonon interactions in R−P-phase layered perovskites and, specifically, the coupling mechanism, strength, and ligand dependence have been studied.[17−20] However, it remains elusive whether vdW interactions or thickness could adjust the electronic and phononic properties as in TMDC and graphene.

In this work, to probe the nonlocal phononic behaviors in layered R−P phase perovskites, we developed vapor-phase epitaxy of single-crystalline $(C_4H_9NH_3)_2PbI_4$ flakes with various thicknesses. As two important indicators, electron−phonon coupling and structural phase transitions were studied by temperature-dependent micro-photoluminescence (PL). Because of the vdW interactions between perovskite layers and from substrates, the structural phase-transition temperature was reduced by >150 K. With reducing flake thickness from ∼100 to ∼20 nm, electron−phonon (longitudinal optical,

LO) coupling strength decreased by ∼30%, indicating long-range interlayer vibrations enabled by interlayer vdW interactions. These non-layered-like electron−phonon interactions in layered perovskites reveal the major influence of vdW interactions and may shed light on low-dimensional perovskite systems on a reduced scale.

Phonon Effects in Epitaxial Ruddlesden−Popper Halide Perovskites at Reduced Dimension. Figure 1a shows the layered structure of $(C_4H_9NH_3)_2PbI_4$ and the electronic and vibrational energy levels of corresponding parts. Although the insulating nature of organic ligands is well known, whether vibrations could pass through or couple across the vdW gap (shown in red) remains unclear. Because the Raman signals from soft crystals are rather weak, more facile methods are needed to probe the vibrational behaviors. (See Supporting Information S2 for more discussion.)

One method we propose is checking electron−phonon coupling strength from PL line width. The predominant coupling mechanism, the Fröhlich interaction formulated in Figure 1b, scales inversely with LO phonons' wavevector, H_{Fr}
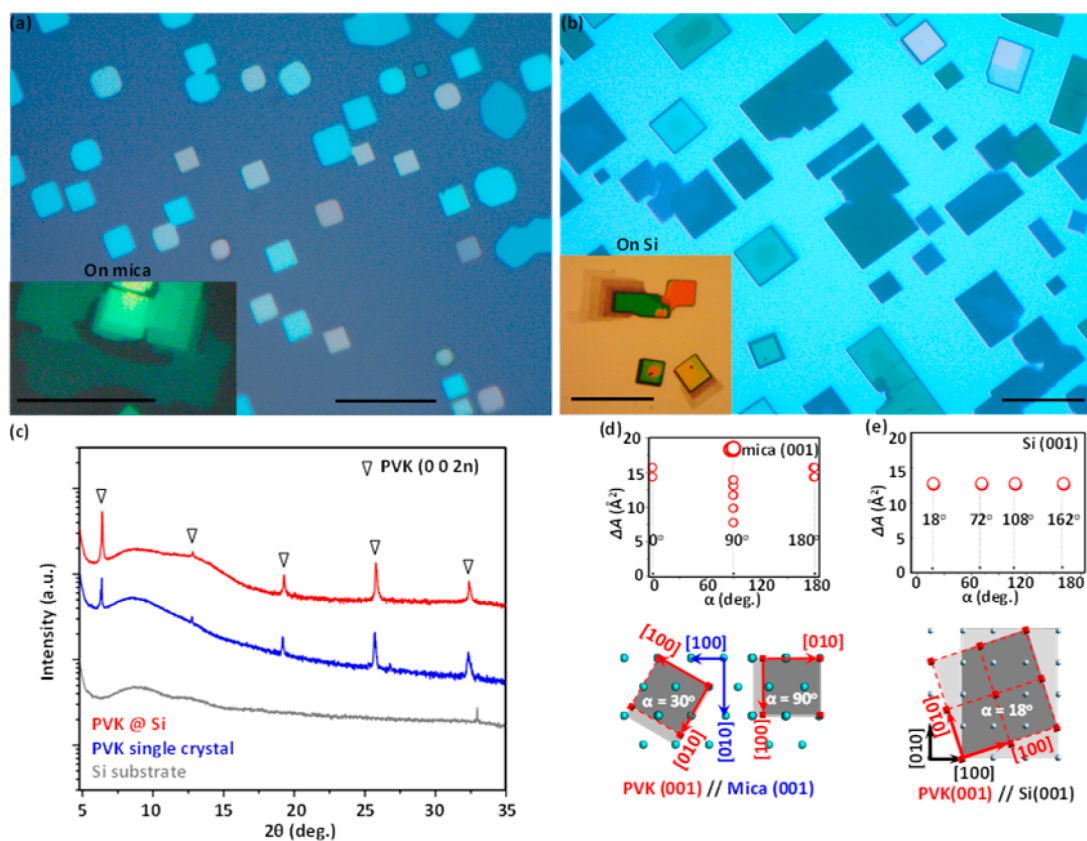
Figure 2. van der Waals epitaxy of $(C_4H_9NH_3)_2PbI_4$. (a,b) $(C_4H_9NH_3)_2PbI_4$ flakes grown on muscovite mica and Si (001), respectively. The insets are enlarged images of step structures showing the layer-by-layer growth. All scale bars are 20 μm. (c) XRD of $(C_4H_9NH_3)_2PbI_4$ flakes grown on Si, bulk $(C_4H_9NH_3)_2PbI_4$ single-crystal and bare Si substrate. (002n) peaks are highlighted. (d,e) Lattice registration between $(C_4H_9NH_3)_2PbI_4$ and mica and Si substrates calculated from GSAM. The lower drawings sketches the predicted lattice registration. The lattice points of mica, Si and perovskites are shown as light-blue, gray, and red dots, respectively. Crystallographic directions of mica, Si, and perovskites are shown by dark-blue, black, and red arrows, respectively. More discussion can be found in the main text and Experimental Methods.

$\propto q^{-1}$.[21,22] In this regard, the long-wavelength phonon leads to a higher scattering rate and, in turn, larger PL fwhm. In MQW of group III−V materials like GaAs/AlAs, because of the mismatched phonon frequencies between well and barrier layers, phonons can be partially confined in well layers.[21−26] In vdW $(C_4H_9NH_3)_2PbI_4$, the highly incoherent interface across the vdW gap is obviously not an effective barrier for phonons. If phonons are confined effectively, then PL fwhm should be thickness-independent. If phonon confinement fails, then we should observe lower PL fwhm in thinner flakes because the LO phonon wavelength is still limited by the thickness of flakes.

For the second method, similar to the aforementioned case of WSe_2/hBN and single-layer $(C_4H_9NH_3)_2PbI_4$ on SiO_2/Si,[6,27] phonons can also be probed with structural transitions. From a soft mode perspective, when the kinetic energy of a crystal is too low to support certain low-energy (soft) vibration modes, the symmetry of the crystal will decrease, and a phase transition occurs.[11,28] With external perturbation (vdW force from substrate), such energy landscape will change, and the critical temperature, T_c, at which soft modes freeze will shift to T_c', as sketched in Figure 1c. See Supporting Information S2 for more discussion.

Epitaxy of $(C_4H_9NH_3)_2PbI_4$. To minimize the interference from impurities and grain boundaries and also guarantee an intimate contact with substrates, single-crystalline flakes were grown on muscovite mica and Si using cold-wall chemical vapor epitaxy (Figure 2a,b). The detailed methods are shown in the Experimental Methods.[12] Optical images showed uniform color and well-defined (truncated) rectangular shapes with lateral size 5−30 μm. The different colors were attributed to optical interference, indicating that various subwavelength thicknesses were obtained in these flakes. With reducing thickness, the flakes became more translucent, and step-like features were observed, indicating layer-by-layer growth, shown in the insets of Figure 2a,b. X-ray diffraction of $(C_4H_9NH_3)_2PbI_4$ flakes grown on Si, bulk single-crystal, and bare Si substrates are shown in Figure 2c. The (002n) peaks were clearly observed in both flakes and bulk crystals, indicating that $(C_4H_9NH_3)_2PbI_4$ crystallizes with (001) parallel to substrate, consistent with previous reports.[29] Therefore, the edges of rectangular flakes are parallel to [100] or [010] directions. Over 90% of the flakes shown in Figure 2a,b were oriented parallel, indicating that epitaxy has been obtained. On the basis of the optical microscopy and the in-plane orientations of mica (refer to Supporting Information S3 for more details) and Si (known from wafer cutting and the shape of cleaved substrates), we were able to figure out the epitaxial relation between flakes and substrates.

To understand the microscopic causes for such orientations, we calculated the optimized lattice registration between $(C_4H_9NH_3)_2PbI_4$ and substrates based on the geometrical superlattice area mismatching (GSAM) method.[30] Basically, the superlattices of perovskite and substrate were rotated by an
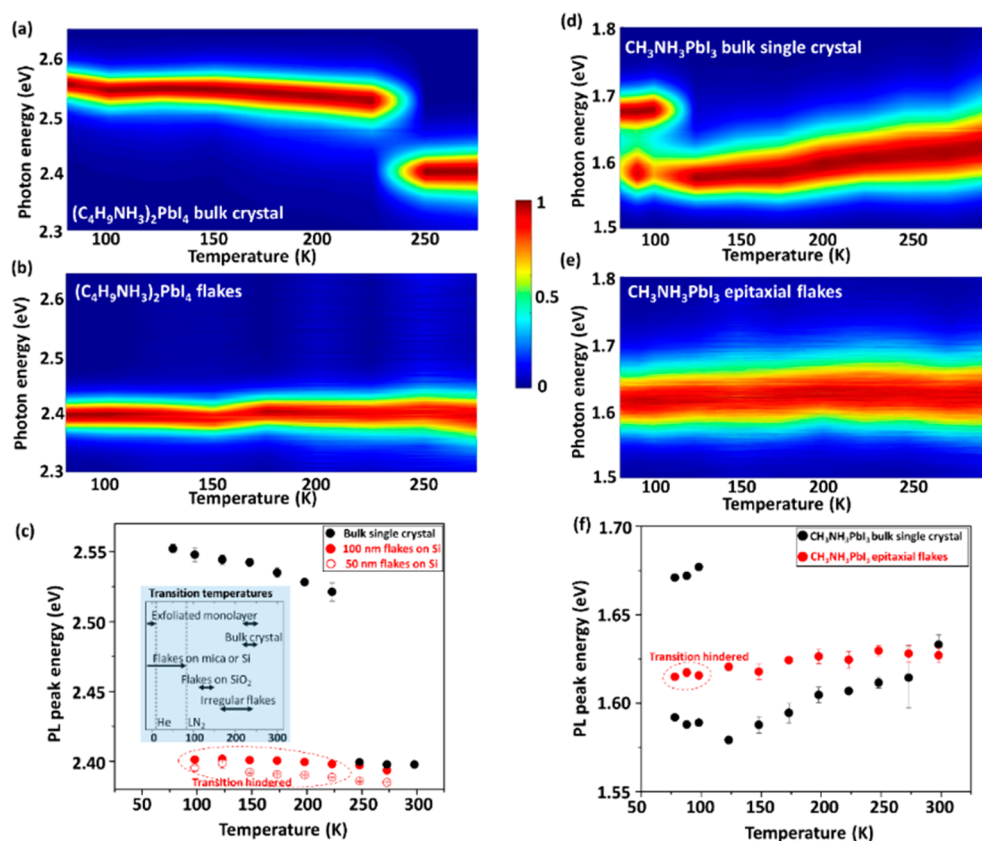
Figure 3. Structural phase transition in 2D $(C_4H_9NH_3)_2PbI_4$ and 3D $CH_3NH_3PbI_3$. (a−c) $(C_4H_9NH_3)_2PbI_4$. (a) Color contour of normalized PL intensity of $(C_4H_9NH_3)_2PbI_4$ bulk single crystal as a function of temperature. The normal phase transition was observed at ∼240 K. (b) Normalized PL intensity of $(C_4H_9NH_3)_2PbI_4$ flakes. The phase transition was locked by vdW interactions from substrate. (c) PL peak energy as a function of temperature in $(C_4H_9NH_3)_2PbI_4$ ∼50 nm, ∼100 nm, and bulk samples. Phase transitions in all epitaxial flakes were locked. The inset showed the phase-transition temperature of different $(C_4H_9NH_3)_2PbI_4$ samples. The dashed lines mark liquid-nitrogen and helium temperature. (d−f) $CH_3NH_3PbI_3$. (d) Normalized PL intensity of $CH_3NH_3PbI_3$ bulk single crystal as a function of temperature. The normal phase transition was observed at ∼110 K. (e) Normalized PL intensity of $CH_3NH_3PbI_3$ flakes. The phase transition was also locked by vdW interactions from substrate. (f) PL peak energy as a function of temperature in $CH_3NH_3PbI_3$.

in-plane angle α. By maximizing the superlattices' overlap, the optimized orientation is obtained. The mismatched area ΔA as a function of in-plane rotation α is plotted in Figure 2d,e. The size of the circle is inversely proportional to the superlattice area. The smaller the ΔA and the larger the circle (superlattice area), the more favorable the alignment. All of the predicted orientations were observed experimentally, indicating that vdW epitaxy does exist between $(C_4H_9NH_3)_2PbI_4$ and Si/mica. (See the Experimental Methods and Supporting Information S4 for more discussion.)

Structural Phase Transition in Epitaxial $(C_4H_9NH_3)_2PbI_4$. The structural phase transition of $(C_4H_9NH_3)_2PbI_4$ was studied by temperature-dependent PL. As a comparison, we synthesized the bulk single crystal of $(C_4H_9NH_3)_2PbI_4$ by the solution method.[31] As shown in Figure 3a, the PL peak position of bulk single crystal $(C_4H_9NH_3)_2PbI_4$ blue-shifted from around 2.40 to 2.53 eV upon cooling, consistent with previous reports.[27] The fact that this diffusionless phase transition proceeded rapidly in bulk single crystal indicates that kinetic effects like nucleation and heat conduction do not cause a significant delay of phase transition in bulk sizes. As expected, the phase transition in epitaxial flakes was locked (Figure 3b). Such phase locking might reduce the transition temperature T_c even lower because some exfoliated flakes were reported to remain in the high-temperature phase, even at

liquid helium temperature (∼4 K).[27] Phase transitions in different samples were further quantified in Figure 3c. Flakes with uniform color, typically green or yellow, showed thickness around 100 nm or higher, whereas those translucent ones like the gray step-like structure in the inset were ∼50 nm. (Refer to Supporting Information S5 for AFM results.) Hereafter we will refer to these two categories of flakes on Si as "50 nm flakes" and "100 nm flakes".

The inset of Figure 3c summarizes T_c of various $(C_4H_9NH_3)_2PbI_4$ samples. The absence of phase transition in exfoliated flakes rules out the size effect as a potential cause for reduced T_c. Rectangular flakes were also grown on 300 nm SiO_2/Si substrates. Probably due to the reduced interaction with amorphous SiO_2 surface, the T_c was only partially reduced, and most flakes transitioned from 120 to 150 K. Some single-domain flakes by chemical vapor deposition (CVD) showed uniform color but failed to reach equilibrium shape. (Refer to Supporting Information S6 for details.) T_c of these nonequilibrium flakes ranged from 160 to 240 K. From these comparisons, a positive correlation between the contact with the substrate and phase locking is clearly revealed; the vdW interaction is strong enough to lock the phase transition of around 40 layers (>100 nm) of $(C_4H_9NH_3)_2PbI_4$. See Supporting Information S7 for more discussions.
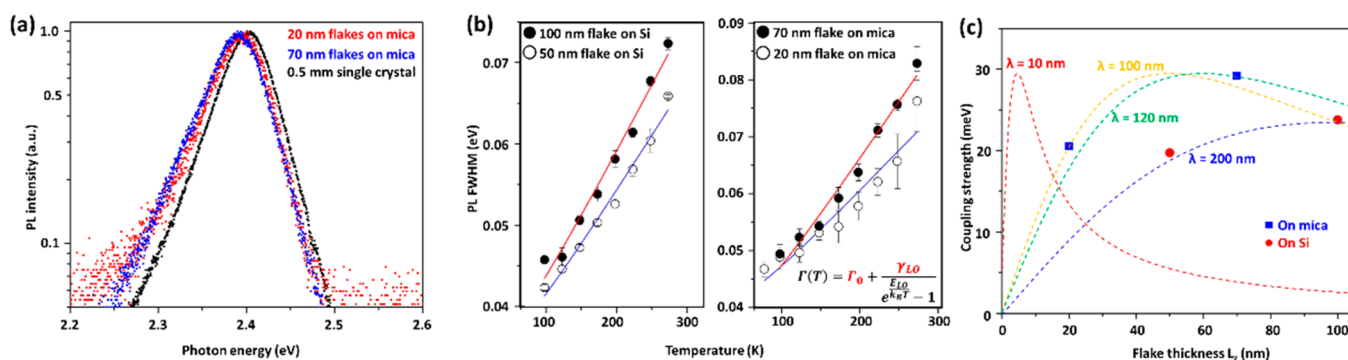
Figure 4. Electron–phonon coupling strength in $(C_4H_9NH_3)_2PbI_4$ flakes with different thickness. (a) Normalized room-temperature PL line shape of $(C_4H_9NH_3)_2PbI_4$ flakes and bulk single crystals. No PL shoulder was observed at lower energy side. (b) Temperature-dependent PL fwhm in $(C_4H_9NH_3)_2PbI_4$ flakes with different thickness. Left panel, on Si; right panel, on mica. (c) Electron–phonon coupling strength as a function of flake thickness, L_z. The four dashed curves are the estimated coupling strengths with different effective phonon wavelengths ranging from 10–200 nm.

As a comparison, we also grew 3D $CH_3NH_3PbI_3$ flakes by vdW epitaxy.[32] See Supporting Information S7 for more discussion. Substrate vdW forces can be transferred much more effectively by 3D $CH_3NH_3PbI_3$. As shown in Figure 3d–f, the same phase transition delay was observed around 110 K, indicating the non-negligible impact from interlayer interactions in 2D $(C_4H_9NH_3)_2PbI_4$.

Electron–Phonon Coupling in Epitaxial $(C_4H_9NH_3)_2PbI_4$. It is generally believed that Pb–I bond (vibration energy ~100 cm^{-1}) is the main cause for the electron–phonon coupling in Pb–I-based compounds.[18,19,33,34] As shown in Figure 4a, the room-temperature PL spectra of 20 and 70 nm $(C_4H_9NH_3)_2PbI_4$ flakes grown on mica and single crystals are compared. The three curves showed a similar asymmetric shape, and no broad shoulder appeared at the low-energy side, indicating that different samples in this study are pure and homogeneous and are free from reabsorption effects. Therefore, PL fwhm in this work is determined intrinsically by electron–phonon coupling, whereas the influence from other extrinsic factors is negligible. See Supporting Information S7 for more discussions.

The electron–phonon coupling is characterized by the phenomenological formula[17,33,35]

$$\Gamma(T) = \Gamma_0 + \gamma_{AC}T + \frac{\gamma_{LO}}{e^{E_{LO}/k_BT} - 1} + \Gamma_{imp}e^{-E_b/k_BT} \quad (1)$$

The four terms stand for inhomogeneous broadening, acoustic phonon scattering, Fröhlich interaction, and scattering from impurities, respectively. γ_{LO} is the phonon coupling strength, and the denominator stands for LO phonon population. E_{LO} means LO phonon energy (100 cm^{-1}).[17] E_b represents the impurity binding energy. Both the impurity term and the acoustic term were ignored in this work.[17,33] (See Supporting Information S8 for more discussion.) The temperature-dependent PL fwhm of $(C_4H_9NH_3)_2PbI_4$ flakes (all locked in high-temperature phase) with different thickness is shown in Figure 4b and is fitted by eq 1. In both panels of Figure 4b, the red curves, which correspond to thicker flakes, are steeper than the blue curves, which fit the thinner flakes. With temperature approaching 80 K, the fwhm narrowing gradually decelerates and might be related to the onset of acoustic phonon scattering. As summarized in Table 1, the LO coupling strength of thicker flakes was higher than those in thinner flakes. All LO coupling strengths distributed between 20 and

Table 1. Fitting Results of Different $(C_4H_9NH_3)_2PbI_4$ Samples

sample	γ_{LO} (meV)	γ_{LO} standard error (meV)	Γ_0 (meV)	Γ_0 standard error (meV)
20 nm on mica	20.54	2.26	40.72	2.04
70 nm on mica	29.16	1.79	38.03	1.70
50 nm on Si	19.72	1.00	35.32	0.95
100 nm on Si	23.77	1.34	36.23	1.28

30 meV, comparable to previous values. All of the inhomogeneous broadening terms ranged between 35 and 41 meV, indicating that all flakes had similar crystal quality.

A previous study on AlGaAs/GaAs and InGaAs/GaAs single quantum well (QW) showed that once phonons were confined in the well layer, the coupling strength yields[26]

$$|H_{Fr}|^2 \propto \frac{L_z}{L_z^2q^2 + \pi^2} \quad (2)$$

where the square of the Fröhlich Hamiltonian $|H_{Fr}|^2$ is proportional to coupling strength, L_z stands for the well thickness, and q stands for the effective wavevector of LO phonon. (See Supporting Information S8 for more discussion.) As sketched in Figure 1b, because the interlayer vibrations have been proved to be delocalized, some long-wave vibration modes could involve multiple layers. Thus it is fair to consider the top and bottom surfaces of each $(C_4H_9NH_3)_2PbI_4$ flake (not individual layer) as the phonon barrier. The whole flake should be treated as a single QW, and flake thickness becomes the well thickness L_z in eq 2. Because the strength of Fröhlich scattering is proportional to phonon wavelength, we ignore the contribution from short-wave phonons and assume that there is only one single phonon mode in each flake.

The L_z dependence is summarized in Figure 4c, where $|H_{Fr}|^2$ is sketched with different LO phonon wavelengths. As shown in Figure 4c, various q are substituted into eq 2 to estimate the effective phonon wavelength in $(C_4H_9NH_3)_2PbI_4$. For each assumed wavelength, the maximum coupling strength is reached when L_z and phonon wavelength are close. In our case, the effective phonon wavelength in flakes grown on mica and Si turned out around 120 and 200 nm, respectively. These values are on the same order as those reported in AlGaAs/GaAs single quantum wells.[26] The fact that the calculated effective wavelength exceeds L_z indicates that the in-plane phonon component also contributed to the electron–phonon

coupling processes. Although the precise microscopic picture of electron−phonon coupling in $(C_4H_9NH_3)_2PbI_4$, especially that across the vdW gap, remains unknown, the phenomenological estimations in this work are sufficient to reveal the nontrivial interlayer interactions in layered $(C_4H_9NH_3)_2PbI_4$.

In addition to chemical composition[36,37] and dielectric environment,[27,38,39] vdW forces in epitaxy provide another method for manipulating the various properties of layered R−P halide perovskites. Strain engineering,[40] a conventional approach,[41] remains to be developed in these systems.

In conclusion, vdW interlayer interactions are nontrivial for the optoelectronic and vibrational properties of layered materials. In this work, by checking the change in structural phase transition and size dependence of electron−phonon coupling, we probed the non-layered-like behaviors in single-crystalline layered Ruddlesden−Popper perovskite $(C_4H_9NH_3)_2PbI_4$ enabled by nontrivial interlayer vdW forces. Single-crystalline $(C_4H_9NH_3)_2PbI_4$ flakes with lateral size 5−30 μm and thickness 20−100 nm were grown on Si and mica by vdW epitaxy. Because of the vdW interaction with the substrates, the structural phase-transition temperature of the $(C_4H_9NH_3)_2PbI_4$ flakes was reduced by >150 K. The interlayer vdW force was found to be strong enough to stabilize over 40 layers of $(C_4H_9NH_3)_2PbI_4$. By temperature-dependent PL studies, we discovered a thickness-dependent electron−phonon coupling (Fröhlich interaction), which indicates nontrivial phonon coupling across vdW gaps in layered $(C_4H_9NH_3)_2PbI_4$. We further estimated that the effective LO phonon wavelength in flakes is around 100−200 nm, comparable to those in AlGaAs/GaAs single quantum wells. Similar to some layered materials, the layered perovskite $(C_4H_9NH_3)_2PbI_4$ behaves to a large extent like nonlayered materials.

EXPERIMENTAL METHODS

The growth of the R−P-phase halide perovskite was conducted in a customized cold-wall chemical vapor deposition system. The coevaporation of PbI_2 and $C_4H_9NH_2 \cdot HI$ was applied to provide vapor-phase precursors for epitaxial growth of flakes on both Si (001) and muscovite mica (001) substrates. Optical microscopy images were obtained by a Nikon Ti−S inverted optical microscope. A Panalytical X'pert PRO MPD XRD was used to reveal the crystal structure of the flakes and their epitaxial relations with substrates. Temperature-dependent PL spectra were collected by a customized optical spectroscopy system in which a Picoquant 405 nm laser was used as an excitation source. Non-contact-mode AFM was used to reveal the surface morphologies of the flakes. A Renishaw 2000 Raman spectrometer and a Zeiss Supra EDX were used to confirm the phase and composition of the crystals, respectively. The GSAM method was applied to simulate the epitaxial relation between flakes and substrates. More details of the experimental methods are given in the Supporting Information.

ASSOCIATED CONTENT

Ⓢ Supporting Information

The Supporting Information is available free of charge on the ACS Publications website at DOI: 10.1021/acs.jp-clett.8b02763.

> Experimental methods, the effect of organic ligand on phase-transition temperatures, Raman spectrum of 2D perovskites, introduction to phonon confinement and

soft mode theory, X-ray pole figure of mica, additional optical images and AFM results, temperature-dependent PL spectra, optical and structural characterizations on 3D perovskites, energy-dispersive spectroscopy of 2D perovskites, and some discussions on fitting model and scattering rates calculation (PDF)

AUTHOR INFORMATION

Corresponding Authors
*J.S.: E-mail: shij4@rpi.edu.
*E.A.W.: E-mail: wertze@rpi.edu.

ORCID
Yiping Wang: 0000-0001-7626-3278
Xin Sun: 0000-0001-5633-3371
Yi-Yang Sun: 0000-0002-0356-2688
Hanwei Gao: 0000-0001-8085-8178
Jian Shi: 0000-0003-2115-2225

Notes
The authors declare no competing financial interest.

REFERENCES

(1) Geim, A. K.; Grigorieva, I. V. Van der Waals Heterostructures. *Nature* 2013, 499, 419.

(2) Tongay, S.; Sahin, H.; Ko, C.; Luce, A.; Fan, W.; Liu, K.; Zhou, J.; Huang, Y.-S.; Ho, C.-H.; Yan, J.; et al. Monolayer Behaviour in Bulk ReS2 due to Electronic and Vibrational Decoupling. *Nat. Commun.* 2014, 5, 3252.

(3) Zhong, M.; Zhang, S.; Huang, L.; You, J.; Wei, Z.; Liu, X.; Li, J. Large-Scale 2D PbI2 Monolayers: Experimental Realization and Their Indirect Band-Gap Related Properties. *Nanoscale* 2017, 9 (11), 3736−3741.

(4) Zhang, X.; Qiao, X.-F.; Shi, W.; Wu, J.-B.; Jiang, D.-S.; Tan, P.-H. Phonon and Raman Scattering of Two-Dimensional Transition Metal Dichalcogenides from Monolayer, Multilayer to Bulk Material. *Chem. Soc. Rev.* 2015, 44 (9), 2757−2785.

(5) Jiang, J.-W.; Tang, H.; Wang, B.-S.; Su, Z.-B. Raman and Infrared Properties and Layer Dependence of the Phonon Dispersions in Multilayered Graphene. *Phys. Rev. B: Condens. Matter Mater. Phys.* 2008, 77 (23), 235421.

(6) Jin, C.; Kim, J.; Suh, J.; Shi, Z.; Chen, B.; Fan, X.; Kam, M.; Watanabe, K.; Taniguchi, T.; Tongay, S.; et al. Interlayer Electron−Phonon Coupling in WSe2/hBN Heterostructures. *Nat. Phys.* 2017, 13, 127.

(7) Lui, C. H.; Liu, L.; Mak, K. F.; Flynn, G. W.; Heinz, T. F. Ultraflat Graphene. *Nature* 2009, 462, 339.

(8) Zhang, H.; Zhang, D.; Lu, X.; Liu, C.; Zhou, G.; Ma, X.; Wang, L.; Jiang, P.; Xue, Q.-K.; Bao, X. Origin of Charge Transfer and Enhanced Electron−Phonon Coupling in Single Unit-Cell FeSe Films on SrTiO3. *Nat. Commun.* 2017, 8 (1), 214.

(9) Stoumpos, C. C.; Cao, D. H.; Clark, D. J.; Young, J.; Rondinelli, J. M.; Jang, J. I.; Hupp, J. T.; Kanatzidis, M. G. Ruddlesden−Popper Hybrid Lead Iodide Perovskite 2D Homologous Semiconductors. *Chem. Mater.* 2016, 28 (8), 2852−2867.

(10) Blancon, J.-C.; Tsai, H.; Nie, W.; Stoumpos, C. C.; Pedesseau, L.; Katan, C.; Kepenekian, M.; Soe, C. M. M.; Appavoo, K.; Sfeir, M. Y. Extremely Efficient Internal Exciton Dissociation Through Edge States in Layered 2D Perovskites. *Science* 2017, 355, 1288.

(11) Dove, M. T. Theory of Displacive Phase Transitions in Minerals. *Am. Mineral.* 1997, 82 (3−4), 213−244.

(12) Chen, Z.; Wang, Y.; Sun, X.; Guo, Y.; Hu, Y.; Wertz, E.; Wang, X.; Gao, H.; Lu, T. M.; Shi, J. Van der Waals Hybrid Perovskite of High Optical Quality by Chemical Vapor Deposition. *Adv. Opt. Mater.* **2017**, *5* (21), 1700373.

(13) Saparov, B.; Mitzi, D. B. Organic−Inorganic Perovskites: Structural Versatility for Functional Materials Design. *Chem. Rev.* **2016**, *116* (7), 4558−4596.

(14) Chen, Z.; Guo, Y.; Wertz, E.; Shi, J. Merits and Challenges of Ruddlesden−Popper Soft Halide Perovskites in Electro-Optics and Optoelectronics. *Adv. Mater.* **2018**, 1803514.

(15) Ogawa, T.; Kanemitsu, Y. *Optical Properties of Low-Dimensional Materials*; World Scientific: 1995; Vol. 2.

(16) Dou, L.; Wong, A. B.; Yu, Y.; Lai, M.; Kornienko, N.; Eaton, S. W.; Fu, A.; Bischak, C. G.; Ma, J.; Ding, T.; Ginsberg, N. S.; Wang, L.-W.; Alivisatos, A. P.; Yang, P. Atomically Thin Two-Dimensional Organic-Inorganic Hybrid Perovskites. *Science* **2015**, *349* (6255), 1518.

(17) Ni, L.; Huynh, U.; Cheminal, A.; Thomas, T. H.; Shivanna, R.; Hinrichsen, T. F.; Ahmad, S.; Sadhanala, A.; Rao, A. Real-Time Observation of Exciton−Phonon Coupling Dynamics in Self-Assembled Hybrid Perovskite Quantum Wells. *ACS Nano* **2017**, *11* (11), 10834−10843.

(18) Straus, D. B.; Hurtado Parra, S.; Iotov, N.; Gebhardt, J.; Rappe, A. M.; Subotnik, J. E.; Kikkawa, J. M.; Kagan, C. R. Direct Observation of Electron−Phonon Coupling and Slow Vibrational Relaxation in Organic−Inorganic Hybrid Perovskites. *J. Am. Chem. Soc.* **2016**, *138* (42), 13798−13801.

(19) Guo, Z.; Wu, X.; Zhu, T.; Zhu, X.; Huang, L. Electron−Phonon Scattering in Atomically Thin 2D Perovskites. *ACS Nano* **2016**, *10* (11), 9992−9998.

(20) Huang, K.; Zhu, B. Dielectric Continuum Model and Fröhlich Interaction in Superlattices. *Phys. Rev. B: Condens. Matter Mater. Phys.* **1988**, *38* (18), 13377−13386.

(21) Cardona, M.; Peter, Y. Y. *Fundamentals of Semiconductors*; Springer: 2005.

(22) Stroscio, M. A.; Dutta, M. *Phonons in Nanostructures*; Cambridge University Press: 2001.

(23) Rudin, S.; Reinecke, T. Electron−LO-Phonon Scattering Rates in Semiconductor Quantum Wells. *Phys. Rev. B: Condens. Matter Mater. Phys.* **1990**, *41* (11), 7713.

(24) Gammon, D.; Rudin, S.; Reinecke, T.; Katzer, D.; Kyono, C. Phonon Broadening of Excitons in GaAs/$Al_xGa_{1−x}$As Quantum Wells. *Phys. Rev. B: Condens. Matter Mater. Phys.* **1995**, *51* (23), 16785.

(25) Qiang, H.; Pollak, F. H.; Sotomayor Torres, C.; Leitch, W.; Kean, A.; Stroscio, M. A.; Iafrate, G. J.; Kim, K. Size Dependence of the Thermal Broadening of the Exciton Linewidth in GaAs/$Ga_{0.7}Al_{0.3}$As Single Quantum Wells. *Appl. Phys. Lett.* **1992**, *61* (12), 1411−1413.

(26) Zhang, B.; Shiraki, Y.; Ito, R. Well Width Dependence of the Exciton Phonon Interaction in Semiconductor Quantum Wells. *J. Phys. Soc. Jpn.* **1994**, *63* (1), 358−362.

(27) Yaffe, O.; Chernikov, A.; Norman, Z. M.; Zhong, Y.; Velauthapillai, A.; van der Zande, A.; Owen, J. S.; Heinz, T. F. Excitons in Ultrathin Organic-Inorganic Perovskite Crystals. *Phys. Rev. B: Condens. Matter Mater. Phys.* **2015**, *92* (4), 045414.

(28) Schneider, T.; Srinivasan, G.; Enz, C. Phase Transitions and Soft Modes. *Phys. Rev. A: At., Mol., Opt. Phys.* **1972**, *5* (3), 1528.

(29) Peng, W.; Yin, J.; Ho, K.-T.; Ouellette, O.; De Bastiani, M.; Murali, B.; El Tall, O.; Shen, C.; Miao, X.; Pan, J.; et al. Ultralow Self-Doping in Two-dimensional Hybrid Perovskite Single Crystals. *Nano Lett.* **2017**, *17* (8), 4759−4767.

(30) Sun, X.; Lu, Z.; Xie, W.; Wang, Y.; Shi, J.; Zhang, S.; Washington, M. A.; Lu, T.-M. Van der Waals Epitaxy of Cds Thin Films on Single-Crystalline Graphene. *Appl. Phys. Lett.* **2017**, *110* (15), 153104.

(31) Chen, Z.; Wang, Y.; Shi, Y.; Hsu, B.; Yang, Z.; Shi, J. Regulating Carrier Dynamics in Single Crystal Halide Perovskite via Interface Engineering and Optical Doping. *Advanced Electronic Materials* **2016**, *2* (10), 1600248.

(32) Wang, Y.; Shi, Y.; Xin, G.; Lian, J.; Shi, J. Two-Dimensional van der Waals Epitaxy Kinetics in a Three-Dimensional Perovskite Halide. *Cryst. Growth Des.* **2015**, *15* (10), 4741−4749.

(33) Wright, A. D.; Verdi, C.; Milot, R. L.; Eperon, G. E.; Pérez-Osorio, M. A.; Snaith, H. J.; Giustino, F.; Johnston, M. B.; Herz, L. M. Electron−Phonon Coupling in Hybrid Lead Halide Perovskites. *Nat. Commun.* **2016**, *7*, 11755.

(34) Fu, J.; Xu, Q.; Han, G.; Wu, B.; Huan, C. H. A.; Leek, M. L.; Sum, T. C. Hot Carrier Cooling Mechanisms in Halide Perovskites. *Nat. Commun.* **2017**, *8* (1), 1300.

(35) Rudin, S.; Reinecke, T.; Segall, B. Temperature-Dependent Exciton Linewidths in Semiconductors. *Phys. Rev. B: Condens. Matter Mater. Phys.* **1990**, *42* (17), 11218.

(36) Mao, L.; Wu, Y.; Stoumpos, C. C.; Traore, B.; Katan, C.; Even, J.; Wasielewski, M. R.; Kanatzidis, M. G. Tunable White-Light Emission in Single-Cation-Templated Three-Layered 2D Perovskites $(CH_3CH_2NH_3)_4Pb_3Br_{10−x}Cl_x$. *J. Am. Chem. Soc.* **2017**, *139* (34), 11956−11963.

(37) Ma, D.; Fu, Y.; Dang, L.; Zhai, J.; Guzei, I. A.; Jin, S. Single-Crystal Microplates of Two-Dimensional Organic−Inorganic Lead Halide Layered Perovskites for Optoelectronics. *Nano Res.* **2017**, *10* (6), 2117−2129.

(38) Chernikov, A.; Berkelbach, T. C.; Hill, H. M.; Rigosi, A.; Li, Y.; Aslan, O. B.; Reichman, D. R.; Hybertsen, M. S.; Heinz, T. F. Exciton Binding Energy and Nonhydrogenic Rydberg Series in Monolayer WS_2. *Phys. Rev. Lett.* **2014**, *113* (7), 076802.

(39) Raja, A.; Chaves, A.; Yu, J.; Arefe, G.; Hill, H. M.; Rigosi, A. F.; Berkelbach, T. C.; Nagler, P.; Schüller, C.; Korn, T.; et al. Coulomb Engineering of the Bandgap and Excitons in Two-Dimensional Materials. *Nat. Commun.* **2017**, *8*, 15251.

(40) Naumis, G. G.; Barraza-Lopez, S.; Oliva-Leyva, M.; Terrones, H. Electronic and Optical Properties of Strained Graphene and Other Strained 2D Materials: A Review. *Rep. Prog. Phys.* **2017**, *80* (9), 096501.

(41) Li, J.; Shan, Z.; Ma, E. Elastic Strain Engineering for Unprecedented Materials Properties. *MRS Bull.* **2014**, *39* (2), 108−114.